Journal of Alloys and Compounds 1065 (2026) 188042

Contents lists available at ScienceDirect

Journal of Alloys and Compounds

journal homepage: www.elsevier.com/locate/jalcom

Lattice strain engineering enabling nickel sulfide for seawater splitting at high current density

You-li Sun [a,1], You-yi Sun [b,1], Yuxuan Zhang [c], Keqiang He [a], Takeshi Yanagida [d,e,*], Johnny C. Ho [c,e,f,*], SenPo Yip [e,**]

[a] Interdisciplinary Graduate School of Engineering Sciences, Kyushu University, Kasuga, Fukuoka 816-8580, Japan
[b] Environmental Science and New Energy Technology Research Center, Tsinghua Shenzhen International Graduate School, Tsinghua University, Shenzhen 518055, PR China
[c] Department of Materials Science and Engineering, City University of Hong Kong, 999077, Hong Kong Special Administrative Region of China
[d] Department of Applied Chemistry, Graduate School of Engineering, The University of Tokyo, Tokyo 113-8656, Japan
[e] Institute for Materials Chemistry and Engineering, Kyushu University, Kasuga-koen 6-1, Kasuga, Fukuoka 816-8580, Japan
[f] City University of Hong Kong (Dongguan), Dongguan 523000, China

ARTICLE INFO

Keywords:
Transition metal sulfides
Strained lattice
Electrocatalyst
Seawater splitting, High current density

ABSTRACT

The instability of transition metal sulfides (TMSs) electrocatalysts poses challenges in seawater splitting, particularly in the oxygen evolution reaction (OER). Lattice strain is an effective strategy to enhance the performance of TMSs. In this work, a lattice-strained Ni_3S_2 (NiFeCoS-LS) was synthesized via a facile room-temperature strategy, where the effective incorporation of Fe and Co induces substantial lattice strain that significantly improves the resistance to Cl^--induced corrosion during alkaline seawater oxidation. As a result, the NiFeCoS-LS catalyst exhibits exceptional long-term stability, maintaining stable performance for over 300 h at a current density of 0.5 A cm^{-2} in alkaline seawater electrolysis. In contrast, the hydrothermally synthesized NiFeCoS (NiFeCoS-HT), which lacks lattice strain, exhibits significantly reduced stability. The enhanced performance arises from the improved thermodynamic stability of Ni_3S_2 induced by lattice strain, which reinforces its structural robustness under operating conditions. Supported by theoretical calculations, the reconstruction and corrosion resistance behavior of NiFeCoS-LS were further elucidated. This work provides mechanistic insights into designing corrosion-resistant TMS-based electrocatalysts for effective seawater electrolysis.

1. Introduction

Electrocatalytic water splitting powered by renewable energy sources, such as solar and wind energy, stands out as a practical and environmentally friendly approach [1–4]. Most hydrogen production via water electrolysis relies on ultra-high-purity water as the electrolyte feedstock, posing significant challenges, particularly in regions with limited freshwater availability. Thus, direct seawater electrolysis has attracted increasing attention as a promising strategy for hydrogen production in arid regions [5–8]. However, this process faces significant challenges due to the high concentration of inorganic ions, such as Ca^{2+}, Mg^{2+}, and Cl^- in seawater [9,10]. These ions can deactivate electrocatalysts over time, and the aggressive Cl^- ions can trigger the unwanted chlorine evolution reaction (CER), which competes with the OER at the anode, thereby impeding efficient hydrogen generation [5]. As a result, these challenges significantly hinder the practical feasibility and large-scale commercialization of seawater electrolysis technologies.

To overcome these challenges, it is crucial to develop robust electrocatalysts that offer high selectivity, strong corrosion resistance, and long-term stability in seawater environments. Although noble metal-based catalysts like Ir and Ru show excellent activity for both the hydrogen evolution reaction (HER) and OER, their effectiveness in seawater is severely hindered by Cl^- poisoning and corrosion [11,12]. Moreover, their scarcity and high cost limit their applicability for large-scale applications. As a result, there is growing interest in non-precious transition metals such as Ni, Fe, Co, Cu, Cr, and Mo, which

* Corresponding authors at: Institute for Materials Chemistry and Engineering, Kyushu University, Kasuga-koen 6-1, Kasuga, Fukuoka 816-8580, Japan
** Corresponding author.
E-mail addresses: yanagida@g.ecc.u-tokyo.ac.jp (T. Yanagida), johnnyho@cityu.edu.hk (J.C. Ho), yip.sen.po.472@m.kyushu-u.ac.jp (S. Yip).
[1] contribution equally to this work

https://doi.org/10.1016/j.jallcom.2026.188042
Received 23 January 2026; Received in revised form 12 April 2026; Accepted 13 April 2026
Available online 15 April 2026

have been integrated into a variety of catalytic systems, including hydroxides, oxides, nitrides, sulfides, phosphides, as well as alloys. Substantial progress has been made, with excellent performance achieved in various transition metal-based seawater splitting systems [13,14], through strategies such as intrinsically "chlorophobic" electrocatalysts [15,16], Cl^--repelling/blocking layers [17–19], and self-reconstructing electrocatalysts [17,18], which demonstrating promising results.

Among the various categories of electrocatalysts, transition metal sulfides (TMSs) have garnered significant attention due to their facile synthesis, natural abundance, unique electronic structures, and excellent electrocatalytic activity [7,20]. Various synthetic strategies have been developed, and the sulfurization of metal precursors is one of the most widely used methods [21]. This approach can preserve the original morphology of the precursor, such as nanowires, nanosheets, or porous structures, thereby enhancing the surface area and maximizing the exposure of active sites, which is beneficial for electrocatalytic applications [7,22]. Their application in seawater splitting has also been widely explored, and despite their excellent performance, their stability under harsh, high-current-density conditions remains one of the most critical challenges for large-scale applications [7,23]. During operation, metal sulfides undergo surface reconstruction into oxyhydroxides under anodic conditions. Meanwhile, the high concentration of Cl^- (~0.5 M) in seawater can infiltrate defective or non-uniform oxide layers, accelerate localized corrosion, and destabilize the partially oxidized surface layer. Under high-current-density conditions, such continuous reconstruction leads to material loss, cracking, and detachment of the catalyst layer [24]. Therefore, strategies to improve structural stability and corrosion resistance are urgently needed. Strategies like lattice strain engineering [25–27], heterointerface engineering [10,28], defect introduction [29], and multiphase composite hybridization [7,30] are widely explored to enhance electrocatalytic performance. Among them, lattice strain engineering is widely employed to modulate the physical and chemical properties of inorganic materials [31,32]. In practice, compressive strain shortens the interatomic distance, enhances orbital overlap, and strengthens chemical bonding, thereby improving the stability of the material [32].

Here, NiFeCoS is used as a model system to investigate how lattice strain can greatly enhance the stability of seawater electrolysis under high-current-density conditions. In this work, lattice-strained NiFeCoS (NiFeCoS-LS) was synthesized *in situ* on nickel foam (NF) substrates through sulfurization of metal layered double hydroxide (MLDH) precursor using a room-temperature soaking method. Compared with the hydrothermally synthesized NiFeCoS (NiFeCoS-HT), NiFeCoS-LS exhibits remarkable oxidation resistance and thermodynamic robustness, maintaining superior stability at commercial current density of 0.5 A cm^{-2} in a saline environment, significantly outperforming NiFeCoS-HT. Density functional theory (DFT) calculations further reveal that the reconstructed structure synergistically enhances the ionic selectivity of the catalyst. This study presents a lattice-strain engineering strategy to enhance the durability of NiFeCoS for alkaline seawater electrolysis, and provides valuable guidance for the development of high-performance materials for high-current-density seawater splitting.

2. Experimental section

2.1. Synthesis of NiFeCo LDH

Before material synthesis, NF (1 × 3 cm) was soaked in 2 M HCl under sonication for 20 min to remove the surface oxides, followed by rinsing with deionized (DI) water. To prepare the NiFeCo LDH precursor solution, 60 mg of $Fe(NO_3)_3{\cdot}9H_2O$ and 80 mg of $Co(NO_3)_2{\cdot}6H_2O$ were dissolved in a mixture of 15 mL of DI water and 5 mL of ethanol. The pre-treated NF was immersed in the solution and left undisturbed for 24 h at room temperature. Afterward, the sample was removed, rinsed, and dried to obtain NiFeCo LDH [33].

2.2. Synthesis of hydrothermally synthesized NiFeCo LDH (NiFeCo LDH-HT)

NiFeCo LDH-HT was synthesized by a hydrothermal method. Specifically, 0.3 g of $Ni(NO_3)_2{\cdot}6H_2O$, 0.1 g of $Fe(NO_3)_3{\cdot}9H_2O$, 0.1 g of $Co(NO_3)_2{\cdot}6H_2O$, 0.3 g of $CO(NH_2)_2$ (urea), and 0.1 g of KCl were dissolved in 20 mL of DI water. The pre-treated NF was immersed in the solution, and the mixture was sealed in a Teflon-lined stainless steel autoclave and maintained at 120 °C for 6 h. After cooling to room temperature, the NF was removed, washed thoroughly with DI water, and dried to obtain NiFeCo LDH-HT.

2.3. Synthesis of NiFeCoS-LS

NiFeCoS-LS was prepared by sulfurization. The as-synthesized NiFeCo LDH was dispersed in 50 mL of DI water together with 168 mg of Na_2S. After stirring for 30 min to obtain a uniform suspension, the mixture was transferred to a Teflon-lined reactor and heated at 120 °C for 3 h. After cooling to room temperature, the sample was washed with DI water and dried to obtain NiFeCoS-LS [33].

2.4. Synthesis of NiFeCoS-HT

NiFeCoS-HT was synthesized by hydrothermal sulfurization of the NiFeCo LDH-HT precursor. In a typical procedure, NiFeCo LDH-HT was placed into a Teflon-lined stainless steel autoclave containing 168 mg of Na_2S dissolved in 50 mL of DI water. The mixture was then heated at 120 °C for 6 h. After cooling to room temperature, the product was collected, washed with DI water several times, and dried to obtain NiFeCoS-HT [34,35].

2.5. Electrochemical measurements

Electrochemical measurements were performed using a Gamry 5000 P electrochemical workstation with a three-electrode system. Linear sweep voltammograms (LSVs) were obtained at a scan rate of 10 mV s^{-1}. The system employed a graphite rod, a Hg/HgO electrode, and a NF coated with the catalyst as the counter, reference, and working electrodes, respectively. Electrochemical impedance spectroscopy (EIS) measurements were performed over a frequency range of 20 kHz to 0.01 Hz at 1.45 V vs. RHE with an amplitude of 10 mV. Long-term durability was assessed using chronopotentiometry measurements in alkaline saline and alkaline seawater. The overall water splitting performance was evaluated using a two-electrode configuration with a PMX18–2A system (Kikusui Electric Industries Co., Ltd.). The conversion of the working potential to the reversible hydrogen electrode (RHE) scale is expressed by the equation: $E_{RHE} = E_{Hg/HgO} + 0.098 + 0.059 \times pH$.

2.6. Materials characterization

Surface morphology and elemental information were acquired from a field-emission scanning electron microscope (FE-SEM, JEOL) equipped with energy-dispersive spectroscopy (EDS, JED-2300). Transmission electron microscopy (TEM) images were collected using a Thermo Fisher STEM. X-ray diffraction (XRD) analysis was conducted to determine the crystal structure of the catalysts using a SmartLab (Rigaku Co., Ltd.), which was equipped with Cu Kα radiation (λ = 1.5406 Å) at a scanning step of 2° min^{-1}. X-ray photoelectron spectroscopy (XPS, EscaLab Xi^+) was conducted to investigate the surface chemical states of the catalysts. An Avio 220 Max inductively coupled plasma optical emission spectrometer (ICP–OES) was used to analyze the elemental composition of the samples. The concentration of the produced hypochlorite was determined by ultraviolet-visible spectrophotometry (UV–Vis). Quasi in situ Raman spectroscopy was performed using a standard three-electrode system and a laser with a wavelength of 532 nm.

3. Results and discussion

NF was selected as the substrate due to its porous structure, large effective surface area, and high electrical conductivity, which facilitates charge transfer and bubble diffusion during the OER process [36]. Ni_3S_2 is widely utilized as a catalyst and battery material owing to its low cost and excellent electrochemical performance (Fig. 1a), and doping can further enhance its physicochemical properties. Fig. S1a (Supporting Information) presents a schematic of the two-step method used to synthesize NiFeCoS-LS and NiFeCoS-HT nanosheets on NF. The detailed procedure is presented in the Experimental section. As shown in Fig. 1b, the XRD patterns of both NiFeCoS-LS and NiFeCoS-HT samples exhibit characteristic diffraction peaks corresponding to Ni_3S_2 (PDF No. 44–1418). The diffraction peaks at 20.7°, 31.3°, 37.8°, 49.8°, and 55.2° are assigned to the (101), (110), (003), (113), and (122) crystal planes of Ni_3S_2, respectively. Notably, in comparison to NiFeCoS-HT, the diffraction peaks of NiFeCoS-LS display a slight rightward shift of ~0.2°, which can be attributed to lattice contraction of Ni_3S_2 induced by the incorporation of Fe and Co [26,37,38]. Among the three metal atoms (Ni, Fe, and Co), the atomic radii follow the order of Fe > Co > Ni. Therefore, the incorporation of Fe and Co into the Ni_3S_2 phase introduces compressive lattice strain, resulting in shorter interatomic distances, as evidenced by the rightward shift of the characteristic XRD peaks. This compressive strain enhances orbital overlap and strengthens the M–S bonding, thereby improving the structural stability and electronic coupling of the catalyst. The surface morphologies of the two sulfides were further characterized by SEM, revealing distinct structural differences. As shown in Fig. S1b, NiFeCoS-LS exhibits a rough and porous surface composed of aggregated nanosheets. This morphology increases the specific surface area and promotes exposure of active sites, which is favorable for electrochemical reactions. In contrast, NiFeCoS-HT (Fig. S1c) displays a dense and uniformly distributed porous structure, also indicative of a high surface area. Such an architecture provides an abundance of catalytic sites, thereby enhancing its electrocatalytic performance [39–41].

To further examine the microstructure and crystal structure of NiFeCoS-LS and NiFeCoS-HT, TEM characterization was performed. As shown in Figs. 1c and 1e, both samples exhibit layered nanostructures. Specifically, NiFeCoS-LS displays a uniform and layered morphology (Fig. 1c), indicating a single-phase microstructure. In contrast, distinct

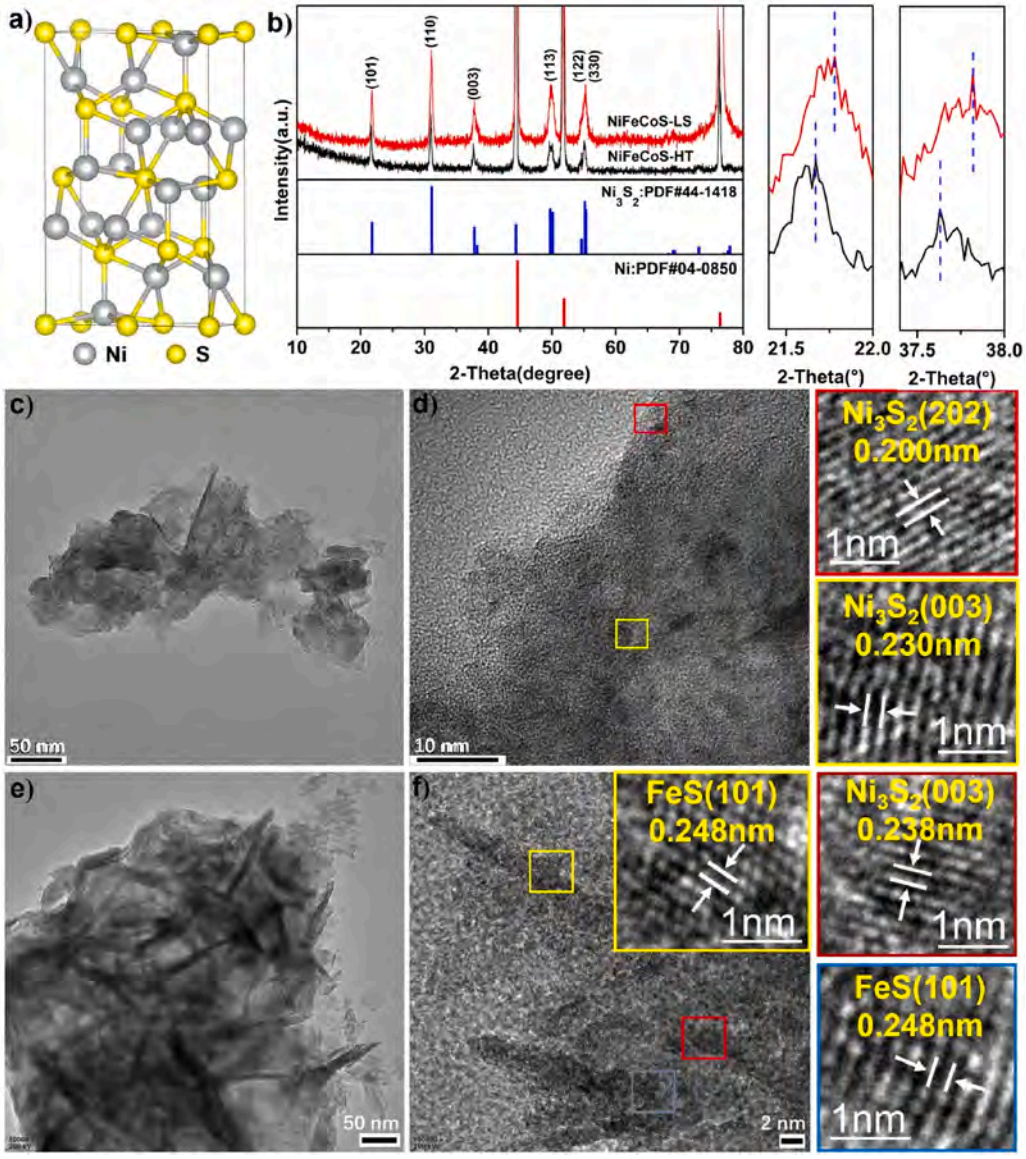

Fig. 1. Crystal structure and microstructure. a) Crystal structure of Ni_3S_2. b) XRD patterns of NiFeCoS-LS and NiFeCoS-HT. c,e) TEM images of NiFeCoS-LS and NiFeCoS-HT. d,f) HR-TEM images of NiFeCoS-LS and NiFeCoS-HT. (insets: HR-TEM images showing the (003), (101), and (202) facets).

nanoneedle and nanosheet structures were observed in the TEM image of NiFeCoS-HT (Fig. 1e), indicating its multiphase nature. High-resolution TEM (HRTEM) was employed to determine the lattice spacings of the two materials. The inverse fast Fourier transform (IFFT) images derived from the selected lattice regions are provided in Fig. S2, which further confirm the well-resolved lattice fringes. For NiFeCoS-LS (Fig. 1d), interplanar spacings of 0.230 nm and 0.200 nm correspond to the (003) and (202) facets of Ni_3S_2. Compared with standard Ni_3S_2, the reduced lattice spacing can be attributed to lattice contraction caused by the incorporation of Fe and Co, which is consistent with the XRD results [42,43]. In the nanosheet phase of NiFeCoS-HT (Fig. 1f), lattice spacings of 0.238 nm and 0.248 nm were indexed to the (003) plane of Ni_3S_2 and the (101) plane of FeS (PDF No. 49–1632), respectively. The well-resolved lattice fringes in the IFFT images (Fig. S2) also indicate that NiFeCoS-LS exhibits shorter interplanar spacings than NiFeCoS-HT. The larger lattice spacing likely indicates that the incorporation of Fe and Co is less efficient than in the NiFeCoS-LS sample. Additional TEM analysis (Fig. S3, Supporting Information) further confirmed that the nanoneedle structures consisted of FeS, with an interplanar spacing of 0.248 nm assigned to the (101) plane of FeS. Furthermore, no crystalline Co-rich phases were detected. Overall, TEM analysis confirms that NiFeCoS-LS is a lattice-strained Ni_3S_2 induced by the incorporation of Fe and Co, whereas NiFeCoS-HT, which lacks lattice strain, is a heterostructure consisting of Ni_3S_2 nanosheets and FeS nanoneedles. Moreover, TEM-EDS mapping (Fig. S4, Supporting Information) shows a homogeneous distribution of Ni, Fe, Co, and S across both materials. ICP-OES analysis (Table S1, Supporting Information) provided quantitative elemental ratios of Ni:Fe:Co ≈ 17:2:1 for NiFeCoS-LS and 29:1:1 for NiFeCoS-HT.

High-resolution XPS was employed to examine the elemental composition and chemical states of NiFeCoS-LS and NiFeCoS-HT. The XPS spectra reveal distinct binding energies for Ni, Fe, Co, and S, indicating that the two materials possess different ligand field environments. For the Ni 2p spectrum (Fig. 2a), both samples exhibit characteristic Ni $2p_{3/2}$ and Ni $2p_{1/2}$ peaks, accompanied by satellite features [44]. The Fe 2p spectrum (Fig. 2b) shows two primary peaks (Fe $2p_{3/2}$ and Fe $2p_{1/2}$) along with satellite features, while the Co 2p spectrum (Fig. 2c) presents Co $2p_{3/2}$ and Co $2p_{1/2}$ peaks and a prominent satellite peak [42]. The S 2p spectrum of NiFeCoS-LS exhibits two dominant peaks at 161.80 eV (S $2p_{3/2}$) and 164.40 eV (S $2p_{1/2}$), corresponding to metal-sulfur bonds (M–S) [45,46]. A weaker feature at 169.42 eV is assigned to SO_x^{2-} species, likely arising from surface oxidation. In contrast, the S 2p spectrum of NiFeCoS-HT shows slightly shifted peaks at 159.04 eV (S $2p_{3/2}$) and 162.01 eV (S $2p_{1/2}$), reflecting differences in the sulfur chemical environment due to the coexistence of Ni_3S_2 and FeS phases [47]. Quantitative fitting (Fig. 2e) indicates that the ratios of Co^{2+} are higher in NiFeCoS-HT than in NiFeCoS-LS, suggesting that higher-valence metal states are more prevalent on the surface of NiFeCoS-LS [48]. In NiFeCoS-LS, the incorporation of Co promotes the formation of Ni–S–Co bonds. The electron-deficient Co^{3+} species withdraw electron density from S atoms, thereby inducing electron transfer from Ni through the Ni–S bond. Consequently, both Ni and Co adopt higher valence states, while S exhibits an higher binding energy. In contrast, NiFeCoS-HT contains Co mainly in the Co^{2+} state, giving rise to a multiphase heterostructure with relatively weak interactions between Ni, Fe, and Co.

The electrocatalytic performance of the catalysts toward the OER was evaluated in a 1.0 M KOH + 0.5 M NaCl electrolyte at room temperature, taking advantage of their nanoporous structures. Their corresponding MLDH counterparts, namely NiFeCo LDH and NiFeCo LDH-HT, were also examined as references. Among the tested samples,

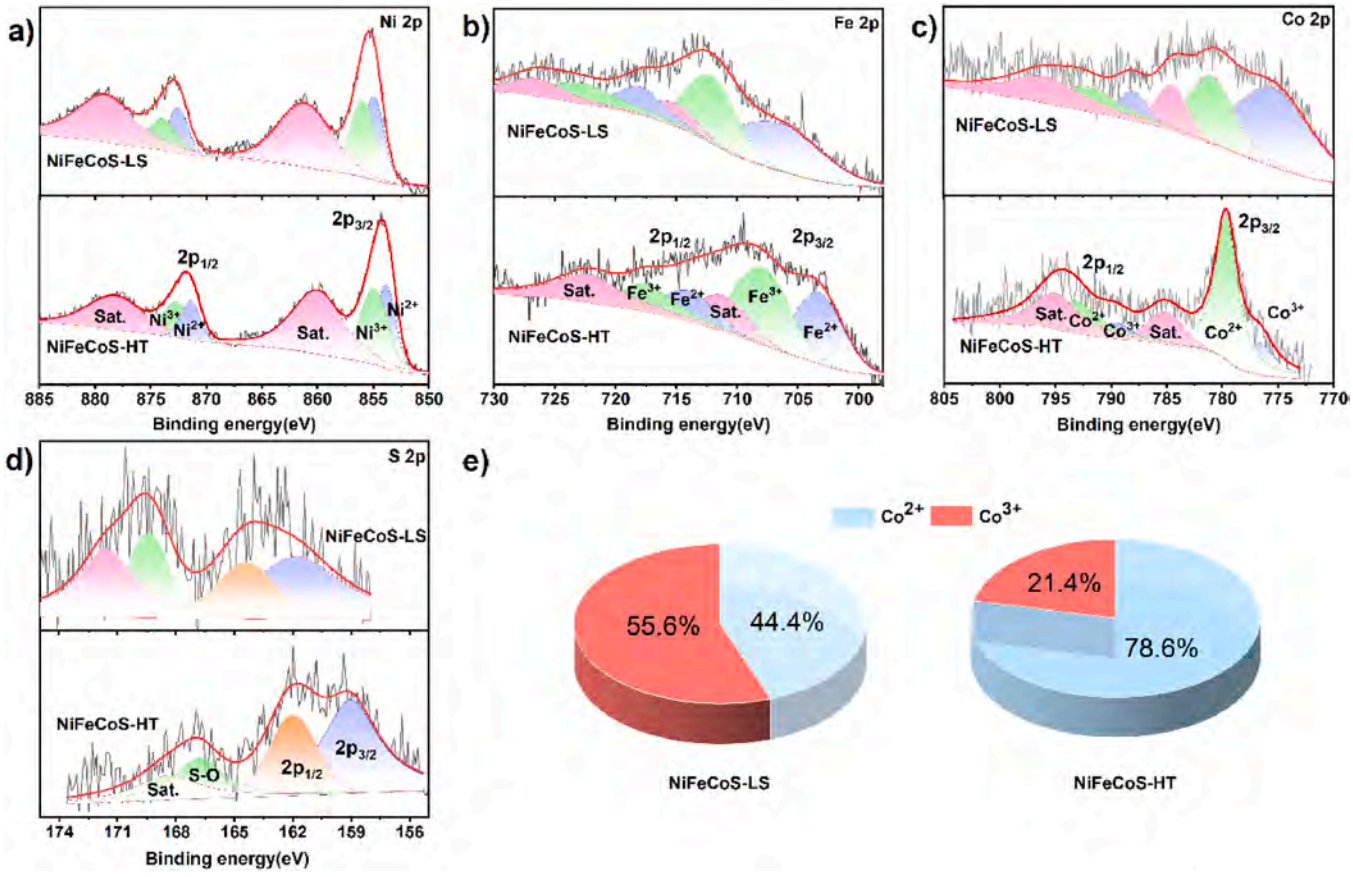

Fig. 2. Surface chemical states of NiFeCoS-LS and NiFeCoS-HT. High-resolution XPS spectra of a) Ni 2p, b) Fe 2p, c) Co 2p, and d) S 2p of the NiFeCoS-LS and NiFeCoS-HT. e) Relative proportions of different Co oxidation states obtained from XPS fitting.

NiFeCoS-LS and NiFeCoS-HT exhibited the best OER activities, delivering overpotentials of 253 and 257 mV, respectively, at 100 mA cm^{-2}, much lower than those of their MLDH counterparts (262 mV for NiFeCo LDH and 310 mV for NiFeCo LDH-HT). The enhanced OER performance can be attributed to the higher electrical conductivity of the metal sulfides compared with their MLDH counterparts, which facilitate more efficient electron transfer on the catalyst surface during the OER process, highlighting the superior activity of the sulfide-based catalysts [49]. At higher current densities, NiFeCoS-LS demonstrated outstanding performance, requiring ultralow overpotentials of 310 and 340 mV to reach current densities of 500 and 1000 mA cm^{-2}, respectively. These values are close to those of NiFeCoS-HT (312 and 340 mV) and significantly smaller than those of NiFeCo LDH (330 and 377 mV) and NiFeCo LDH-HT (393 and 447 mV) under identical conditions (Fig. 3b). To further assess the reaction kinetics, Tafel plots were derived from the polarization curves. As shown in Fig. 3c, NiFeCoS-LS exhibited the lowest Tafel slope (37.61 mV dec^{-1}), followed by NiFeCoS-HT (44.79 mV dec^{-1}), NiFeCo LDH (45.69 mV dec^{-1}), and NiFeCo LDH-HT (49.98 mV dec^{-1}), confirming its faster reaction kinetics due to enhanced adsorption and desorption of oxygenated intermediates. The EIS curves further supported these results (Fig. 3d), NiFeCoS-LS exhibited the lowest charge transfer resistance (0.77 Ω), which is slightly lower than that of NiFeCoS-HT (0.79 Ω), indicating more efficient charge transport. Corrosion resistance was also examined in the same electrolyte. As shown in Fig. 3e, the corrosion potential followed the order: NiFeCoS-LS (0.353 V vs. Hg/HgO) > NiFeCo LDH (0.0216 V vs. Hg/HgO) > NiFeCo LDH-HT (−0.0303 V vs. Hg/HgO) > NiFeCoS-HT (−0.641 V vs. Hg/HgO), confirming the superior corrosion resistance of NiFeCoS-LS. Long-term stability tests further highlighted the robustness of the catalyst in a saline environment: NiFeCoS-LS maintained its activity for 100 h at 0.5 A cm^{-2} with negligible performance degradation (Figs. 3f and 3g), whereas NiFeCoS-HT failed after less than 10 h under the same conditions. These results demonstrate that NiFeCoS-LS exhibits not only excellent catalytic activity and fast OER kinetics but also remarkable resistance to Cl^--induced corrosion, making it a highly promising catalyst for high-current-density seawater electrolysis.

The OER performance of the catalysts was further evaluated in alkaline natural seawater (1.0 M KOH + seawater). As shown in Figs. 4a and 4b, both NiFeCoS-LS and NiFeCoS-HT exhibited remarkable activity, achieving a current density of 0.5 A cm^{-2} at overpotentials of 346 and 350 mV, respectively. These values are significantly lower than those of NiFeCo LDH (370 mV) and NiFeCo LDH-HT (397 mV), highlighting the superior catalytic efficiency of sulfide-based materials [48]. The corrosion resistance of the catalysts in alkaline seawater follows the trend shown in Fig. 4c: NiFeCoS-LS (0.368 V vs. Hg/HgO)

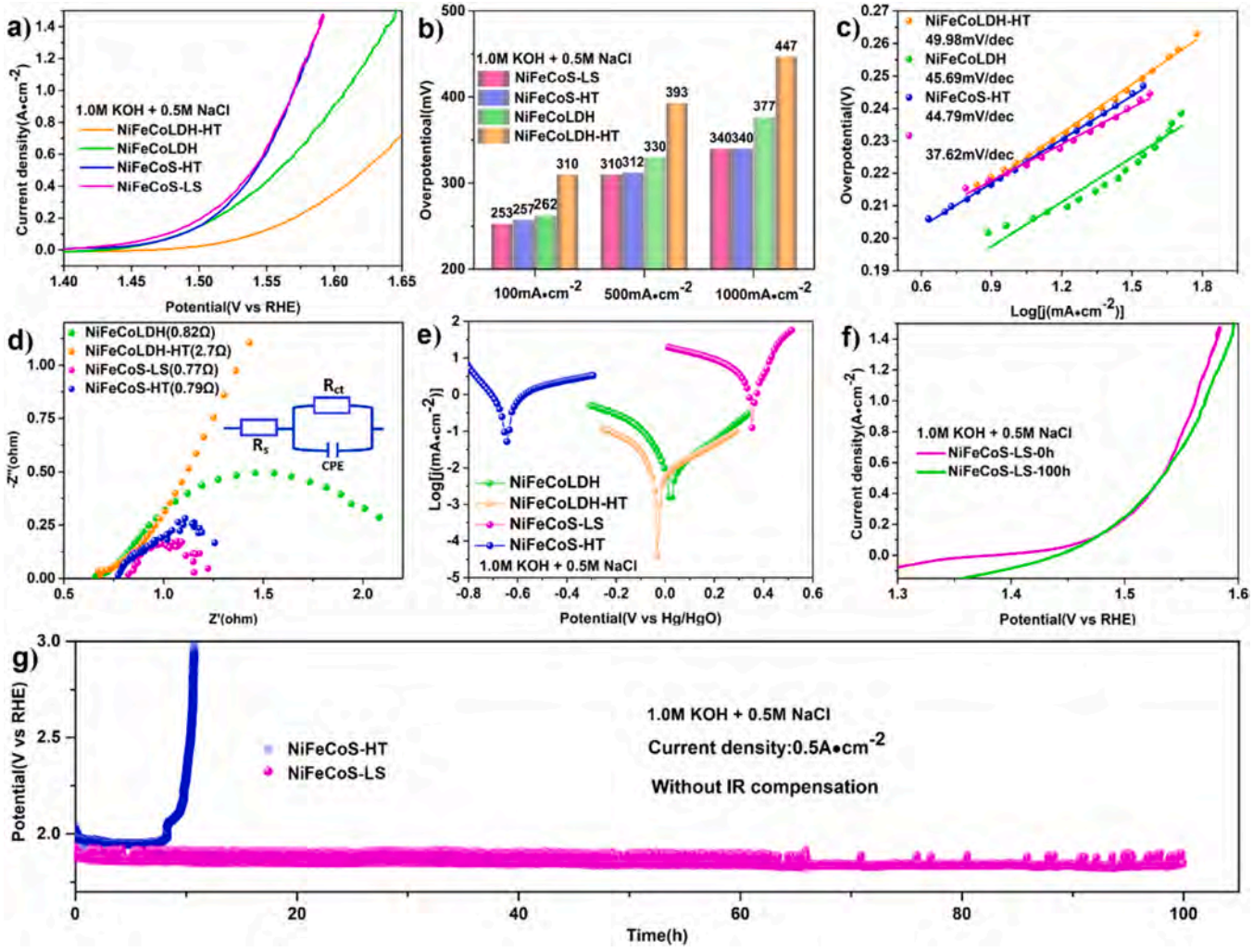

Fig. 3. Electrocatalytic properties evaluated in an alkaline saline electrolyte. a-d) LSV curves, overpotentials, Tafel plots, and EIS curves of NiFeCoS-LS, NiFeCoS-HT, NiFeCo LDH, and NiFeCo LDH-HT electrodes in 1.0 M KOH + 0.5 M NaCl. e) Polarization curves of NiFeCoS-LS, NiFeCoS-HT, NiFeCo LDH, and NiFeCo LDH-HT electrodes. f) LSV curves of the NiFeCoS-LS electrode before and after 100 h of operation. g) Chronopotentiometry tests of NiFeCoS-LS and NiFeCoS-HT electrodes at 0.5 A cm^{-2} without ohmic compensation.

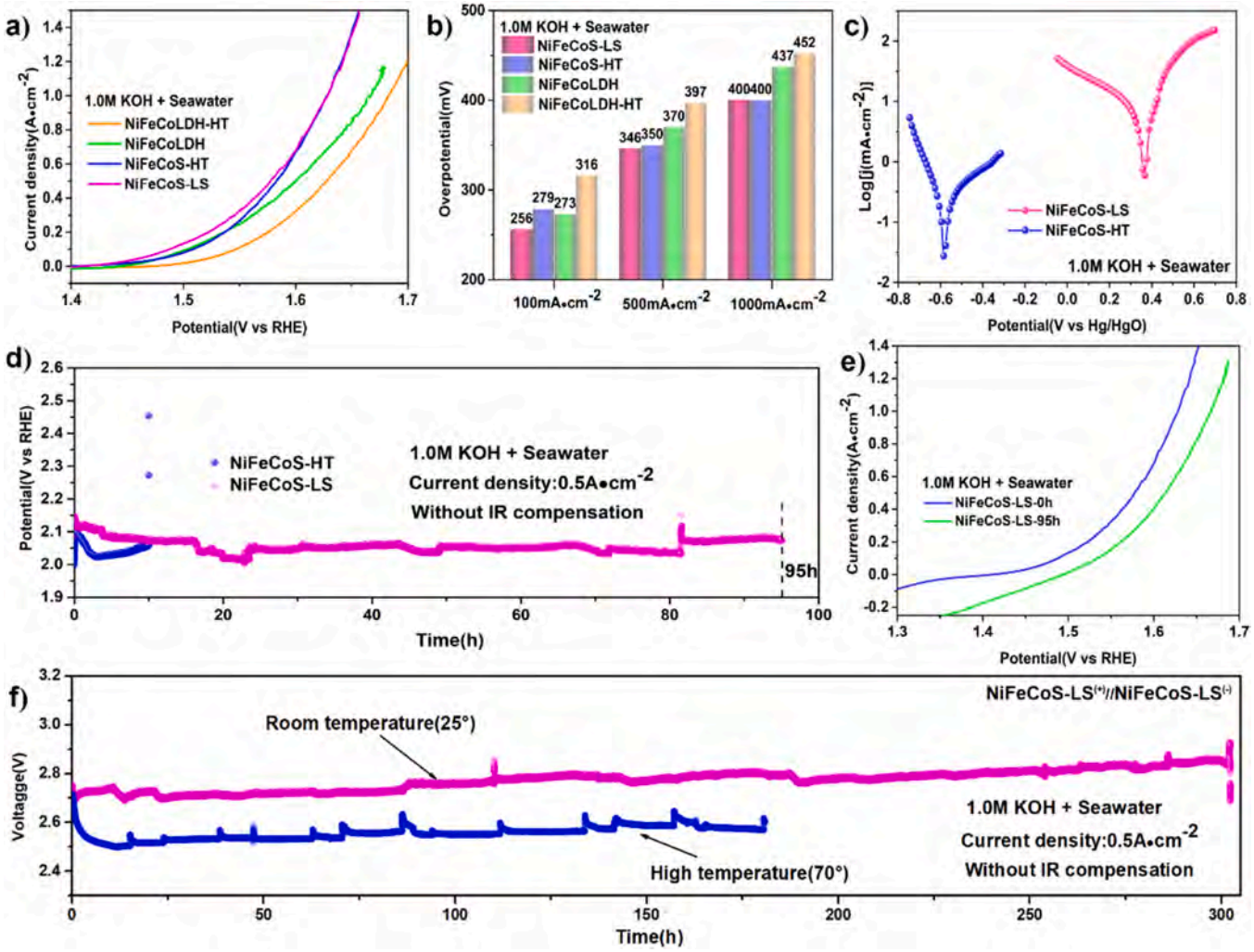

Fig. 4. Electrocatalytic properties evaluated in an alkaline seawater electrolyte. a-b) LSV curves and overpotentials of NiFeCoS-LS, NiFeCoS-HT, NiFeCo LDH, and NiFeCo LDH-HT electrodes in 1.0 M KOH + seawater. c) Polarization curves of NiFeCoS-LS and NiFeCoS-HT electrodes in an alkaline seawater electrolyte. d) Chronopotentiometry test of the NiFeCoS-LS electrode at 0.5 A cm^{-2} without ohmic compensation. e) LSV curves of the NiFeCoS-LS electrode before and after 95 h of operation. f) Chronopotentiometry curves of NiFeCoS-LS || NiFeCoS-LS at 0.5 A cm^{-2} in alkaline natural seawater at different temperatures.

> NiFeCoS-HT (−0.585 V vs. Hg/HgO). The NiFeCoS-LS nanosheets exhibit excellent corrosion resistance, indicating superior robustness for seawater electrolysis. Chronopotentiometry measurements at 0.5 A cm^{-2} (Fig. 4d) further confirm the outstanding electrochemical stability of NiFeCoS-LS, as the catalyst maintains stable operation for 95 h, whereas NiFeCoS-HT shows significant degradation within 10 h. Post-stability LSV measurements (Fig. 4e) confirm that NiFeCoS-LS retains excellent catalytic performance. Performance degradation in seawater is often attributed to the deposition of Ca^{2+} and Mg^{2+} hydroxides, which can block active sites, but NiFeCoS-LS shows minimal impact from this effect within the testing period.

Finally, the overall seawater-splitting performance of NiFeCoS-LS was evaluated in an electrocatalytic cell (Fig. 4f). Here, NiFeCoS-LS was used as both the anode and cathode to examine durability. Notably, the electrochemical cell exhibited excellent operational stability, maintaining consistent performance for 300 h at ambient temperature, thereby highlighting the remarkable long-term durability of the NiFeCoS-LS electrode. The bifunctional electrocatalytic performance of the NiFeCoS-LS electrodes was further assessed at an elevated temperature of 70 °C in a 1 M KOH + seawater electrolyte. As shown in Fig. 4f, the NiFeCoS-LS catalyst exhibited sustained OER activity, maintaining stable performance at a high current density of 0.5 A cm^{-2} for over 180 h at 70 °C, with only negligible performance degradation during the prolonged operation. These results highlight the potential of NiFeCoS-LS nanosheets as industrial electrocatalysts for efficient high-current-density water splitting in freshwater and seawater. The reaction selectivity was evaluated by monitoring ClO^- formation, a product of the competitive CER during seawater electrolysis. UV–vis spectroscopy showed no characteristic ClO^- absorption peaks after 150 h at 0.5 A cm^{-2}, confirming the excellent ion selectivity of NiFeCoS-LS toward the OER (Fig. S5, Supporting Information).

The degradation behavior of NiFeCoS-LS and NiFeCoS-HT in seawater splitting was further investigated after the stability test. Metal sulfides are known to transform into metal oxides or hydroxides during the OER process [50,51]. To investigate the phase evolution of NiFeCoS-LS and NiFeCoS-HT, their crystal structure and chemical states were examined after electrolysis for 20 h in an 1.0 M KOH + 0.5 M NaCl electrolyte (Fig. S6, Supporting Information) at 200 mA cm^{-2} using XRD and XPS. The resulting samples were labeled as NiFeCoS-LS-20 and NiFeCoS-HT-20, respectively. As shown in Fig. 5a, the XRD pattern of NiFeCoS-LS-20 exhibits a distinct Ni_3S_2 diffraction peak with almost no signal from oxidized phases, indicating the antioxidation properties of the lattice-strained sample during OER. In contrast, NiFeCoS-HT-20 shows a very weak Ni_3S_2 (110) peak, along with the appearance of a nickel–iron oxide diffraction peak, suggesting that the heterostructure is more susceptible to oxidation under operating conditions. These results

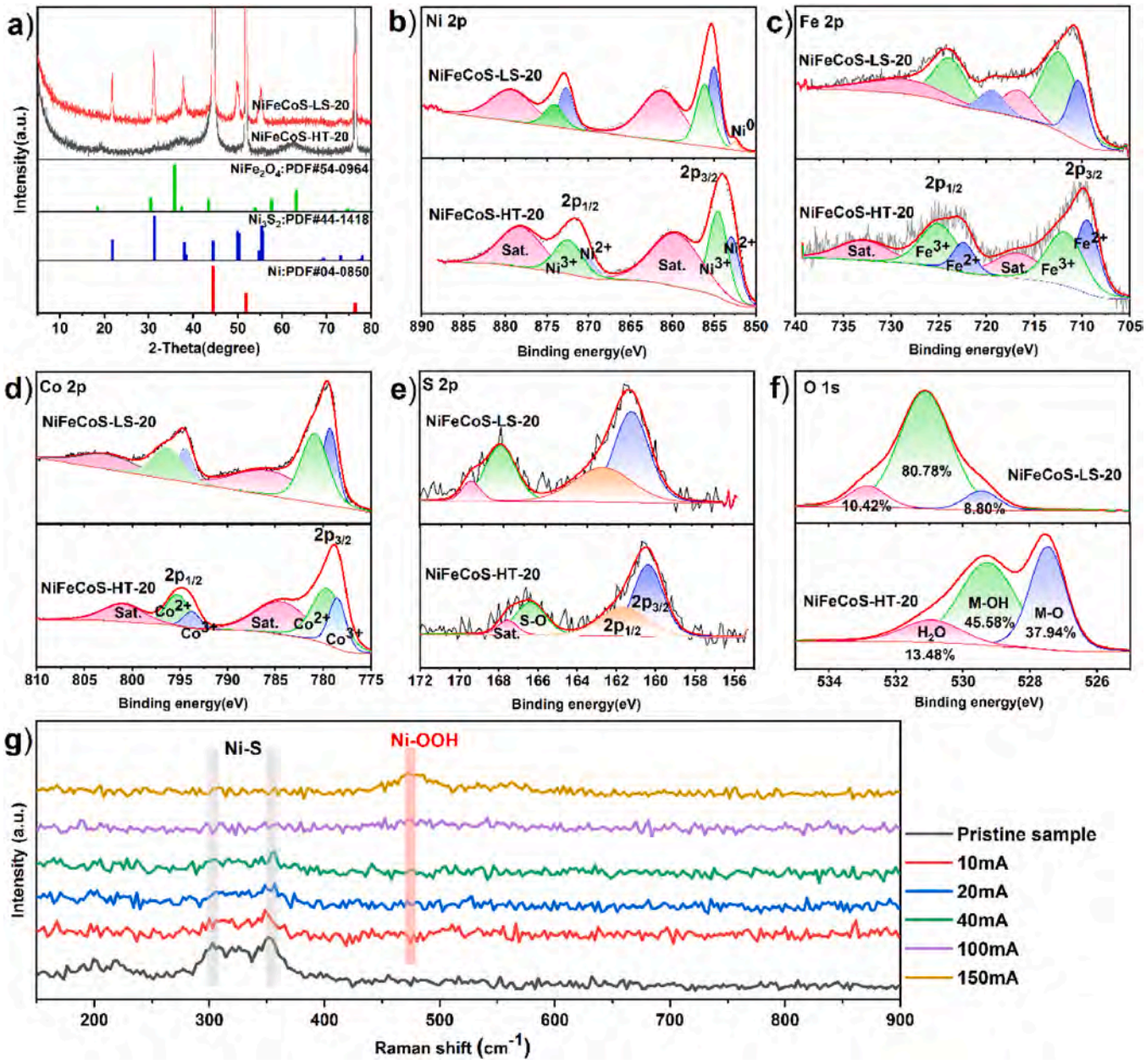

Fig. 5. Crystal structure and surface state characterizations after the stability test. a) XRD patterns of NiFeCoS-LS-20 and NiFeCoS-HT-20. High-resolution XPS spectra of b) Ni 2p, c) Fe 2p, d) Co 2p, e) S 2p, and f) O 1 s of NiFeCoS-LS-20 and NiFeCoS-HT-20. g) In situ Raman spectra of NiFeCoS-LS at different current densities.

indicate that lattice strain and heterojunction engineering lead to markedly different kinetic behaviors. High-resolution XPS was further employed to probe the chemical state changes. In Figs. 5b-5d, the Ni 2p, Fe 2p, and Co 2p spectra of NiFeCoS-LS-20 and NiFeCoS-HT-20 display characteristic $2p_{3/2}$ and $2p_{1/2}$ peaks along with satellite features [52]. The S 2p spectra (Fig. 5e) show peaks at 160–163.2 eV corresponding to M–S, with SO_x^{2-} signals observed, particularly for NiFeCoS-HT-20, indicating mild surface oxidation or partial sulfur loss. The O 1 s spectra (Fig. 5f) of NiFeCoS-LS-20 can be deconvoluted into M–O (529.44 eV), M–OH (531.12 eV), and H_2O (532.85 eV), with M–OH accounting for 80.78%, reflecting a high concentration of surface hydroxyl groups. On the other hand, in NiFeCoS-HT-20, the M-OH fraction decreases to 48.58%, while M–O increases to 37.94%, suggesting a higher degree of oxide formation. These observations confirm that kinetic reconstruction during the OER differs significantly between the materials. The NiFeCoS-LS exhibits exceptional oxidation resistance and anti-reconstruction behavior, whereas the NiFeCoS-HT is more susceptible to surface oxidation and structural changes. Additionally, during seawater electrolysis, NiFeCoS-LS generated minimal deposits at the bottom of the electrolyte after 20 h (Fig. S6, Supporting Information), while NiFeCoS-HT produced substantial black precipitates, reflecting differences in kinetic stability. Fig. 5g presents the quasi *in situ* Raman spectra of the NiFeCoS-LS sample. The characteristic Ni-S peaks, initially located at 304 and 350 cm^{-1}, gradually decrease in intensity with increasing current density. Meanwhile, a new peak appears at 470 cm^{-1}, which is assigned to NiOOH species. This evolution provides direct spectroscopic evidence of the dynamic surface reconstruction of NiFeCoS-LS during the OER, revealing the structural origin of its enhanced catalytic activity.

Based on the detailed characterizations and electrochemical performance results, NiFeCoS-LS and NiFeCoS-HT exhibit distinct microstructures and Cl^--induced corrosion behavior in OER. To reveal the

underlying factors that govern their development, the growth mechanisms were reviewed, and further studies were carried out. For the growth of NiFeCoS-LS, NiFeCo LDH was first formed. Fe^{3+} ions in the precursor are readily hydrolyzed in aqueous solution, thereby generating an acidic environment. Given that the standard electrode potential of Ni ($E^{\circ}_{(Ni^{2+}/Ni)} = -0.257$ V) is lower than that of the nitrate ion ($E^{\circ}_{(NO_3^-/NO)} = 0.96$ V), nickel is etched from the NF surface to form Ni^{2+} ions [53]. Simultaneously, Fe^{3+}, Co^{2+}, and Ni^{2+} ions spontaneously form a polymetallic MLDH on the NF substrate. Subsequent sulfurization in a sodium sulfide solution converts the MLDH into lattice-strained Ni_3S_2. The reactions are summarized in the following equations:

Acid environment generation: $Fe^{3+} + (x + y)H_2O \rightarrow [Fe(OH)_x(H_2O)_y]^{(3-x)+} + xH^+$

The formation of Ni^{2+}: $3Ni + 8H^+ + 2NO_3^- \rightarrow 3Ni^{2+} + 2NO + 4H_2O$

Ionic self − assembly : $Co^{2+} + Ni^{2+} + [Fe(OH)_x(H_2O)_y]^{(3-x)+} + NO_3^- + H_2O \rightarrow NiFeCoLDH$

Sulfurization: NiFeCo LDH + $Na_2S \rightarrow$ NiFeCoS-LS

Here, the Fe^{3+} ions are crucial in stabilizing the MLDH structure, while Co^{2+} ions, with a radius similar to that of Ni^{2+}, readily incorporate into the interlayer, promoting the formation of lattice-strained Ni_3S_2. In contrast, NiFeCo LDH-HT, the precursor of NiFeCoS-HT, is primarily formed under alkaline conditions, which are generated during the hydrolysis of urea at elevated temperatures. The alkaline environment allows the Fe^{3+}, Co^{2+}, and Ni^{2+} ions to co-deposit on NF, forming a polymetallic hydroxide layer, leading to ineffective incorporation of Fe and Co into Ni_3S_2 [54]. An ion-exchange process then transforms these hydroxides into metal sulfides, resulting in a heterostructure of polymetallic sulfides. The reactions are represented in the following equations:

Alkaline environment generation: $NH_2CONH_2 + 3H_2O \rightarrow NH_4^+ + 2OH^- + CO_2$

Ionic co − deposition : $Co^{2+} + Ni^{2+} + Fe^{3+} + OH^- + CO_3^{2-} \rightarrow NiFeCoLDH - HT$

Sulfurization: NiFeCoLDH-HT + $Na_2S \rightarrow$ NiFeCoS-HT

The distinct growth pathways of the two sulfides account for their differing structural features and differences in performance. The material characterizations further support this claim. XRD patterns of both MLDH samples (Fig. S7, Supporting Information) reveal that the (003) diffraction peak of NiFeCo LDH shifts approximately 0.2° to the left. At the same time, NiFeCo LDH-HT displays a clear $Ni(OH)_2$ peak. The XRD results indicate that NiFeCo LDH exhibits lattice expansion [55], while NiFeCo LDH-HT is a heterostructure consisting of multiple phases. High-resolution XPS spectra of Ni, Fe, Co, and O (Fig. S8, Supporting Information) provide additional insights. Both NiFeCo LDH and NiFeCo LDH-HT show Ni $2p_{3/2}$ and Ni $2p_{1/2}$ peaks with satellite features, as shown in the Ni 2p spectrum (Fig. S8a) [52]. The Ni^{2+} peak is more pronounced in NiFeCo LDH-HT, indicating a lower proportion of high-valence Ni and minimal change in valence during deposition [56]. As shown in the Fe 2p spectrum (Fig. S8b), the Fe^{3+} fraction increases while Fe^{2+} decreases in NiFeCo LDH, reflecting the oxidation state adjustments during hydroxide formation [57]. The Co^{3+} peak in the Co 2p spectrum (Fig. S8c) is more pronounced in NiFeCo LDH, suggesting a higher proportion of high-valence Co and a more stable hydroxide structure. The O 1 s spectrum (Fig. S8d) shows that the NiFeCo LDH-HT contains a higher fraction of M–OH, indicating greater hydroxide content on the surface. In contrast, NiFeCo LDH has more oxygen vacancies, which correlates with its superior OER performance [58]. The durability of NiFeCo LDH and NiFeCo LDH-HT was evaluated in 1.0 M KOH + 0.5 M NaCl solution (Fig. S9, Supporting Information). Notably, NiFeCo LDH maintained stable operation for 80 h, highlighting its long-term durability, whereas NiFeCo LDH-HT showed degradation after 8 h of operation. This is attributed to the presence of the $Ni(OH)_2$ and $Fe(OH)_3$ phases in NiFeCo LDH-HT. During saline electrolysis, Cl^- readily corrodes the $Ni(OH)_2$ and $Fe(OH)_3$ phases, leading to the structural collapse of the material and subsequent performance degradation. Overall, these analyses indicate that NiFeCo LDH forms a hydroxide structure with abundant oxygen vacancies and a higher density of active sites. In contrast, NiFeCo LDH-HT primarily generates stable M–OH species, which explains their differences in catalytic behavior. The structural differences induced variations in electrochemical reactions that further extend to their sulfide counterparts, highlighting the importance of suitable synthesis methods for enhancing seawater stability under high-current-density conditions.

The S-O substitution process occurring in the pre-catalytic stage highlights distinct reconstruction pathways for the two NiFeCoS materials, suggesting that the resulting reconstructed structures differ in both configuration and oxygen evolution mechanism (Fig. 6a). Experimental results demonstrate that NiFeCoS-LS exhibits exceptional catalytic performance and corrosion resistance in both alkaline saline and seawater. Its remarkable stability, both thermodynamic and kinetic stability, is attributed to its intrinsic structure and the *in situ* formation of NiFeCoOOH during the OER process [50,59]. This highly stable, corrosion-resistant oxyhydroxide layer protects the inner sulfide layers from rapid oxidation, thereby preserving the structural integrity and activity of the catalyst [59,60]. In contrast, NiFeCoS-HT exhibits weaker interaction forces among heterostructured Ni_3S_2/FeS, resulting in reconstructed NiOOH/FeOOH/CoOOH layers that are more susceptible to Cl^- attack. This vulnerability accelerates degradation during seawater electrolysis, highlighting the importance of lattice strain engineering for robust performance [59,61]. To gain a deeper understanding of the synergistic effects between the multimetallic constituents during the catalytic process after electrocatalytic reconstruction, as well as the adsorption behavior of reaction intermediates at different metal sites, DFT calculations were conducted. For NiFeCoS-LS, the *in situ* reconstructed NiFeCoOOH structure (Fig. S10a, Supporting Information) is highly resistant to Cl^--induced corrosion, which can protect the inner NiFeCoS from rapid phase structural transformation. However, NiFeCoS-HT quickly transforms into corresponding MOOH (Fig. S10b and S10c, Supporting Information) during the OER process. Fig. 6d presents the Cl^- adsorption energies of the three models. The adsorption energy of NiFeCoOOH is −2.32 eV, which is less negative than that of NiOOH (-2.56 eV) and FeOOH (-3.23 eV), indicating that NiFeCoOOH exhibits stronger resistance to Cl^--induced corrosion. Previous theoretical studies have shown that pyrite-type NiS_2 with the incorporation of V, Co, or Ir significantly enhances the binding strength of surface sulfur atoms. The theoretical sulfide oxidation potential (U_{SOR}) and the difference in potential (ΔU) represent the onset potential for reconstruction and the intrinsic reconstructive tendency of metal sulfides, respectively. With the incorporation of V, Co, or Ir, both U_{SOR} and ΔU increase during the OER, indicating delayed reconstruction and improved phase stability [62]. In contrast, the heterostructure sulfides have weaker interatomic bonds and show a much higher tendency for structural reconstruction. These findings underscore that strong metal-metal and metal-sulfur interactions, as present in lattice-strained NiFeCoS, are critical for resisting Cl^- induced corrosion and maintaining long-term catalytic activity during high-current-density seawater electrolysis.

4. Conclusions

In summary, different types of NiFeCoS-based TMS catalysts were synthesized via a sulfurization strategy using metal hydroxide precursors. Experimental and theoretical investigations demonstrate that lattice-strained Ni_3S_2 exhibits superior electrocatalytic activity and exceptional durability in both alkaline saline and natural seawater. This

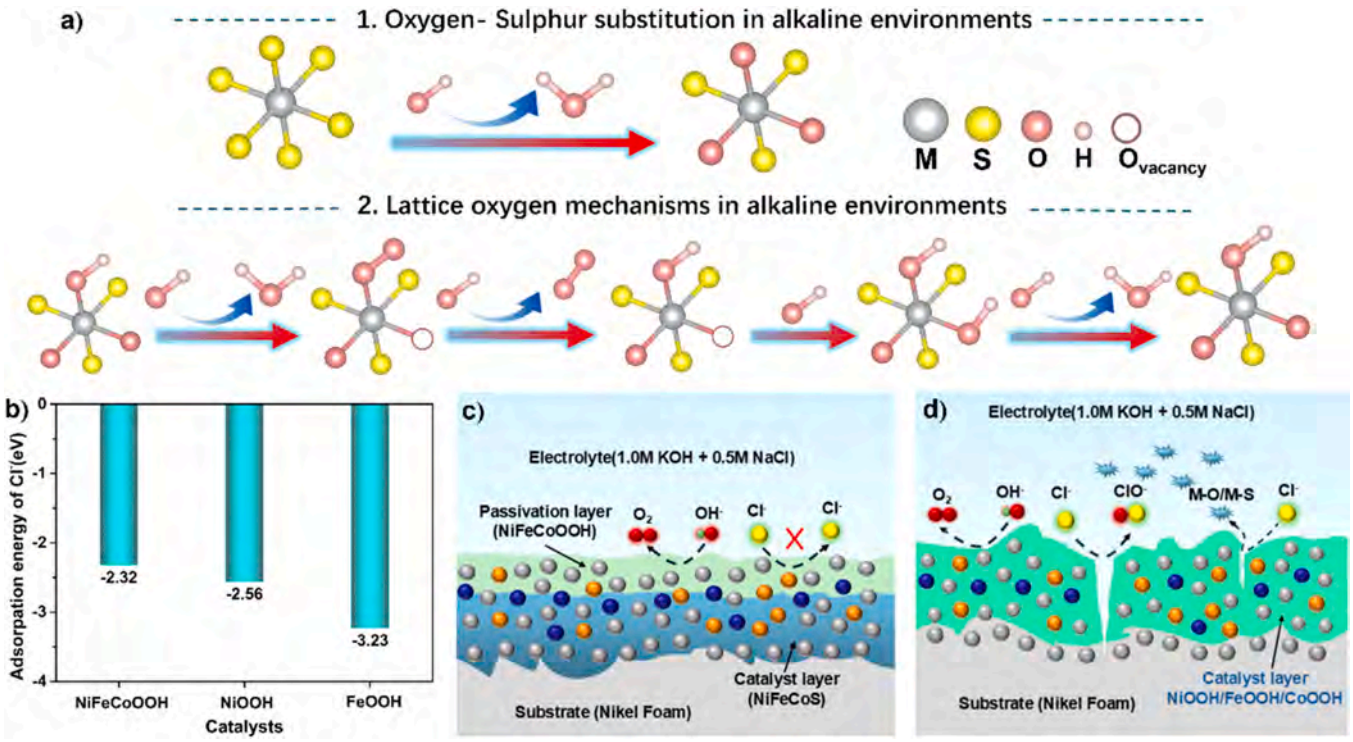

Fig. 6. Mechanism investigation. a) Schematic diagram of the lattice oxygen mechanism with a lattice sulfur-oxygen substitution process. b) Adsorption energies of Cl^-. c,d) Schematic illustrations of the evolution process of NiFeCoS-LS and NiFeCoS-HT in saline solution during the OER.

catalyst maintains high efficiency under prolonged exposure to chloride-rich environments, highlighting its practical potential for seawater electrolysis. In contrast, the heterostructure NiFeCoS-HT suffers rapid degradation due to weaker resistance to chloride-induced corrosion. The observed differences in kinetics and reconstruction behavior underscore the critical role of lattice strain engineering for long-term catalyst stability. While promising performance and durability are achieved through lattice strain engineering in this work, challenges remain for future development. In particular, scale-up may lead to non-uniform current distribution and mass transport limitations, while issues such as gas bubble management, chloride-induced corrosion, and multivalent ion precipitation (e.g., Ca^{2+}, Mg^{2+}) become increasingly critical challenges at even higher current densities and must be addressed in future work. Overall, this work provides valuable insights into the rational design of robust seawater splitting electrocatalysts, highlighting the importance of elemental structural uniformity.

CRediT authorship contribution statement

Johnny C. Ho: Writing – review & editing, Conceptualization. **Takeshi Yanagida:** Writing – review & editing, Conceptualization. **Keqiang He:** Validation, Formal analysis. **Yuxuan Zhang:** Software. **You-yi Sun:** Formal analysis. **You-li Sun:** Writing – original draft, Validation, Methodology, Formal analysis. **Yip Senpo:** Writing – review & editing, Conceptualization.

Declaration of Competing Interest

The authors declare that they have no known competing financial interests or personal relationships that could have appeared to influence the work reported in this paper.

Acknowledgments

The "Network Joint Research Center for Materials and Devices" supported this work by the Ministry of Education, Culture, Sports, Science and Technology (MEXT). The first author is supported by the China Scholarship Council. The authors would like to express their sincere gratitude to Dr. Quan for the support in *in situ* Raman measurements and insightful analysis.

Appendix A. Supporting information

Supplementary data associated with this article can be found in the online version at doi:10.1016/j.jallcom.2026.188042.

Data availability

The data supporting this study's findings are available from the corresponding author upon reasonable request.

References

[1] W. He, Y. Wang, Y. Zhao, C. Tang, L. Cong, C. Wang, Y. Lu, X. Liu, J. Dong, S. Cherevko, Q. Hua, Q. Zhang, Heterointerface-enabled anti-reverse-current electrodes for alkaline water electrolyzers at 1000 mA cm^{-2}, J. Am. Chem. Soc. 148 (2026) 5232–5242.
[2] Y. Sun, Z. Yang, Y. Sun, R. Yu, A.Y. Ganin, Antiperovskite nitrides as efficient and durable electrocatalysts for industrially relevant hydrogen evolution, ACS Catal. 16 (2026) 3135–3148.
[3] R. Lu, B. Wang, L. Li, Z. Bao, B. Li, Q. Du, K. Jiao, Advances in direct seawater electrolysis for green hydrogen production: emerging technologies and future perspectives, Sci. Bull. 71 (2026) 172–195.
[4] A.U. Rehman, M. Asghar, A. Rauf, T. Najam, I.A. Shaaban, S.S.A. Shah, M.A. Nazir, MOF/Graphene interfaces in catalytic water splitting: Recent breakthroughs and future outlook, Fuel 405 (2026) 136800.
[5] Q. Sha, S. Wang, L. Yan, Y. Feng, Z. Zhang, S. Li, X. Guo, T. Li, H. Li, Z. Zhuang, D. Zhou, B. Liu, X. Sun, 10,000-h-stable intermittent alkaline seawater electrolysis, Nature 639 (2025) 360–367.
[6] J. Lu, P.-J. Deng, Y. Liu, S. Jing, P. Tsiakaras, Surface reconstruction of an integrated CoO-Co2Mo3O8 electrode enabling efficient ampere-level hydrogen evolution in alkaline water or seawater, Angew. Chem. Int. Ed. 64 (2025) e202423863.
[7] J. Wang, Y. Liu, G. Yang, Y. Jiao, Y. Dong, C. Tian, H. Yan, H. Fu, MXene-assisted NiFe sulfides for high-performance anion exchange membrane seawater electrolysis, Nat. Commun. 16 (2025) 1319.

[8] P. Wang, Q. Gao, M.-R. Gao, Critical progress in direct seawater electrolysis for sustainable hydrogen production, Chem. Commun. 62 (2026) 3465–3482.
[9] P. Wang, P. Wang, T. Wu, C. Zhao, Z. Pu, Y. Zhang, Interface engineering of NiMoSx@NiMnFe Prussian blue analogue nanowires to efficiently boost overall seawater splitting at high current densities, Adv. Funct. Mater. 35 (2025) 2417924.
[10] P. Tian, W. Zong, J. Xiong, W. Liu, J. Liu, Y. Dai, J. Zhu, S. Huang, S. Song, K. Chu, G. He, N. Han, Dynamic reconstruction of crystal/amorphous hetero-phosphate janus interfaces for highly stable seawater splitting, Adv. Funct. Mater. 35 (2025) 2504862.
[11] S. Liu, S. Wang, S. Liu, Z. Lin, J. Liu, F. Zeng, J. Hu, P. Zhang, Z. Cai, Y. Huang, T. Wang, Q. Li, Promoting oxide pathway mechanism on low-ruthenium-content oxides for enhanced oxygen evolution in proton exchange membrane water electrolyzer, Angew. Chem. Int. Ed. (2026) e8854134.
[12] J. Xu, C.-C. Kao, H. Shen, H. Liu, Y. Zheng, S.-Z. Qiao, Ru0.1Mn0.9Ox electrocatalyst for durable oxygen evolution in acid seawater, Angew. Chem. Int. Ed. 64 (2025) e202420615.
[13] S.S. Roy, S. Nagappan, P. Mazumder, F.D.C. P, V. Vishesh, S. Kundu, Recent advances in non-precious metal catalysts for anion exchange membrane water electrolysis, Dalton Trans. 55 (2026) 540–562.
[14] S. Mishra, N.H. Rathod, G. Agarwal, V. Kulshrestha, Recent advances in bipolar membrane engineering for direct seawater electrolysis: improved efficiency and stability for hydrogen generation, Small 22 (2026) e07739.
[15] C. Das, N. Sinha, A. Nair, S. Pal, K. Joshi, P. Roy, Chlorophobic iron hydrogen phosphite as OER-active electrocatalyst in anion exchange membrane (sea)water electrolysis, Small 21 (2025) 2505781.
[16] J. Mu, C. Yu, X. Song, L. Chen, J. Zhao, J. Qiu, A super-chlorophobic yet weak-reconstructed electrocatalyst by fluorination engineering toward chlorine oxidation-free and high-stability seawater electrolysis, Adv. Funct. Mater. 35 (2025) 2423965.
[17] H. He, Z. Chen, W. Ma, Q. Chen, Q. Li, X. Lv, J. Dang, CuCoCrRuMo HEA achieving Cl^- repulsion and Mg resource recovery in industrial-current-density seawater electrolysis, Acta Mater. 307 (2026) 121971.
[18] W. Shi, Y. Song, Q. Li, J. He, Z. Zhang, X. Zhang, X. Zhang, L. Zhang, Ni(OH)2/NiFe-PBA heterostructure nanoarrays with a surface-reconstructed Cl^- repelling layer for efficient and stable seawater electrolysis, Chem. Commun. 61 (2025) 12389–12392.
[19] R. Liu, Y. Yan, Y. Liu, T. Yang, B. Qin, L. Qiao, W. Cai, X. Zheng, Self-supported N-doped amorphous C layers encapsulated Mo_2C nanocrystals for efficient alkaline seawater hydrogen evolution reaction, J. Alloy. Compd. 1064 (2026) 187834.
[20] X. He, Y. Yao, L. Zhang, H. Wang, H. Tang, W. Jiang, Y. Ren, J. Nan, Y. Luo, T. Wu, F. Luo, B. Tang, X. Sun, Hexafluorophosphate additive enables durable seawater oxidation at ampere-level current density, Nat. Commun. 16 (2025) 4998.
[21] S. Biswal, A. Kumari, B. Mishra, D. Ghosh, B.P. Tripathi, Ferromagnetic synergy in a ruthenium single-atom catalyst on NiCo2S4 for magnetically enhanced water splitting, ACS Catal. (2026).
[22] Y. Dai, X. Tu, K. Yue, Y. Wan, P. Zhao, X. Shi, F. Huang, Y. Yan, Anti-dissolving high entropy phosphorus sulfide for efficient and durable seawater electrolysis, Adv. Funct. Mater. 35 (2025) 2417211.
[23] Y. Tian, J.-B. Chen, J. Ying, G. Tian, Y.-X. Xiao, Y. Lu, S.-M. Wu, W. Geng, L. Shen, X.-Y. Yang, Homologous CoS2 interface with directed electron transfer and strong chloridion repulsion for efficient seawater oxidation, Sci. China Chem. 68 (2025) 1869–1878.
[24] M. Maqsood, S. Zahid, M. Shoaib, A. Tariq, Z. Bibi, T. Ahmad, Y. Su, R. Muhammad Irfan, Splitting oceans for energy: recent advances in catalyst stability for seawater electrolysis, Langmuir 41 (2025) 32237–32254.
[25] W. Wang, Z. Li, J. Wang, Y. Chen, C. Wu, Y.-S. He, C. Shen, N. Liu, K. Wu, L. Chen, Z.-F. Ma, L. Li, Visualization and quantification of lattice strain in battery cathode particles through electron backscatter diffraction imaging, Nat. Commun. 17 (2026) 1421.
[26] M. Zubair, Y. Qian, K.-H. Park, D.J. Kang, Strain-modulated engineering of high-entropy vanadium-based chalcogenide for sustainable water oxidation, Small (2026) e73201.
[27] J. Wang, J. Xiao, J.J.M. Vequizo, T. Hisatomi, M. Nakabayashi, W. Li, D. Lu, J. Chen, N. Shibata, A. Yamakata, K. Domen, Mg-doped nanosized $BaTaO_2N$ with long-lived charge carriers toward efficient overall water splitting, J. Am. Chem. Soc. 148 (2026) 14680–14688.
[28] Y. Zhang, Y. Qi, H. Zhou, Y. Zhang, J. Sun, W. Ma, J. Hu, L. Feng, F. Yu, Built-in electric field engineering in $Co_2N_{0.67}$/CoP heterostructures for glycerol electrooxidation-assisted hydrogen production, Nat. Commun. (2026).
[29] Y. Guo, J. Hong, Q. Dong, H. Liu, Y. Mei, J. Yan, D. Cheng, A. Nie, Q. Wang, P. Li, Y. Yao, J. Lu, Y. Yuan, Highly stable twin defects enabled by high entropy configuration, Angew. Chem. Int. Ed. 65 (2026) e20550.
[30] W. Dai, X. Wang, Y. Ma, S. He, M. Chen, Z. Yin, S. Tian, M. Wang, S. Yu, H. Zhang, Y. Wang, H. Wang, J. Li, F. Gao, B. Cheng, Y. Wang, Z. Yin, D. Ma, 2D phosphides heterostructures on titanium microfiltration membrane for enhanced ampere-level current density overall seawater splitting, Nano Res. 18 (2025) 94907061.
[31] X. Yang, Y. Wang, X. Tong, N. Yang, Strain engineering in electrocatalysts: fundamentals, progress, and perspectives, Adv. Energy Mater. 12 (2022) 2102261.
[32] J. Luo, J. Tong, H. Zhao, X. Zeng, F. Liu, H. Wu, H. Cui, P. Tan, J. Pan, The role of lattice strain in advancing electrocatalytic performance: from mechanisms to practical applications, Nanoscale 18 (2026) 3985–4021.
[33] S. Niu, T. Tang, Y. Qu, Y. Chen, H. Luo, H. Pan, W.-J. Jiang, J. Zhang, J.-S. Hu, Mitigating the reconstruction of metal sulfides for ultrastable oxygen evolution at high current density, CCS Chem. 6 (2023) 137–148.
[34] M. Wang, L. Zhang, Y. He, H. Zhu, Recent advances in transition-metal-sulfide-based bifunctional electrocatalysts for overall water splitting, J. Mater. Chem. A 9 (2021) 5320–5363.
[35] C. Shi, J. Zhou, M.A. Boda, K. Zhao, Z. Yang, D. Yuan, Z. Yi, Boosting hydrogen production from alkaline water splitting via electrochemical active surface reconstruction of transition metal sulfide electrocatalysts, J. Mater. Chem. A 13 (2025) 4538–4549.
[36] X. Wang, X. Xu, Y. Nie, R. Wang, J. Zou, Electronic-state modulation of metallic co-assisted Co7Fe3 alloy heterostructure for highly efficient and stable overall water splitting, Adv. Sci. 10 (2023) 2301961.
[37] X. Zhong, Y. Sun, X. Chen, G. Zhuang, X. Li, J.-G. Wang, Mo doping induced more active sites in urchin-like W18O49 nanostructure with remarkably enhanced performance for hydrogen evolution reaction, Adv. Funct. Mater. 26 (2016) 5778–5786.
[38] Y. Luo, P. Wang, G. Zhang, S. Wu, Z. Chen, H. Ranganathan, S. Sun, Z. Shi, Mn-doped nickel–iron phosphide heterointerface nanoflowers for efficient alkaline freshwater/seawater splitting at high current densities, Chem. Eng. J. 454 (2023) 140061.
[39] Y. Sun, A.Y. Ganin, The synergistic effects of alloying on the performance and stability of Co_3Mo and Co_7Mo_6 for the electrocatalytic hydrogen evolution reaction, Hydrogen 1 (2020) 11–21.
[40] S. Swathi, R. Yuvakkumar, G. Ravi, M. Thambidurai, H.D. Nguyen, D. Velauthapillai, Ternary copper iron sulfide microflowers anchored on reduced graphene oxide for water splitting, ACS Appl. Nano Mater. 6 (2023) 6538–6549.
[41] A.E.A. Aboubakr, A. Sabbah, R. Putikam, M.H. Elsayed, Y. Ahmed, M.-C. Lin, L.-C. Chen, K.-H. Chen, C.-H. Hung, Single-source assisted synthesis of spin-regulated cobalt/nickel co-doped pyrite FeS_2: enhanced spin channels in Co-Ni-Fe oxyhydroxides for efficient alkaline oxygen evolution reaction, Small (2026) e14853.
[42] Y. Yao, C. Yang, S. Sun, H. Zhang, M. Geng, X. He, K. Dong, Y. Luo, D. Zheng, W. Zhuang, S. Alfaifi, A. Farouk, M.S. Hamdy, B. Tang, S. Zhu, X. Sun, W. (Walter) Hu, Boosting alkaline seawater oxidation of cofe-layered double hydroxide nanosheet array by Cr doping, Small 20 (2024) 2307294.
[43] J. Lu, Z. Yu, X. Wei, X. Zhang, X. Wang, K. Liu, Y. Cai, H. Pan, D. Liu, Z. Wang, Fe/Co Co-Doping Engineering for corrosion-resistant and effective seawater electrolysis, Adv. Mater. 38 (2026) e15156.
[44] Y. Zhuo, D. Liu, L. Qiao, S. Chen, J. Lu, W.F. Ip, H. Pan, Z. Wang, Ultrafast room-temperature synthesis of large-scale, low-cost, and highly active Ni—Fe based electrodes toward industrialized seawater oxidation, Adv. Energy Mater. 13 (2023) 2301921.
[45] S.Y. Jung, J. Lee, K. Aydin, J. Jang, C. Ahn, T. Kim, H. Han, Y.K. Jeong, Transition metal sulfide and nickel-iron layered double hydroxide nanohybrids for promising alkaline seawater oxidations, Appl. Surf. Sci. 649 (2024) 159097.
[46] Y. Sun, Y. Sun, Y. Zhang, T. Yanagida, J.C. Ho, S. Yip, Iron-cobalt co-doped nickel sulfides: a robust electrocatalyst for high-current-density seawater splitting, Adv. Funct. Mater. 36 (2026) e17978.
[47] L. Hong, C. Jing, Y. Zhang, H. Huang, Q. Jiang, J. Tang, Heterostructures with transition metal sulfides and transition metal phosphide: NiMnS/FeP achieve efficient seawater OER, J. Environ. Chem. Eng. 13 (2025) 115224.
[48] X. Zhao, X. Shang, Y. Quan, B. Dong, G.-Q. Han, X. Li, Y.-R. Liu, Q. Chen, Y.-M. Chai, C.-G. Liu, Electrodeposition-solvothermal access to ternary mixed metal Ni-Co-Fe sulfides for highly efficient electrocatalytic water oxidation in alkaline media, Electrochim. Acta 230 (2017) 151–159.
[49] Z. Yousefi, A.A. Asgharinezhad, A. Larimi, C. Ghotbi, Highly efficient electrocatalytic water oxidation based on non-precious metal oxides/sulfides derived from a FeCoNi-metal organic framework, J. Alloy. Compd. 1002 (2024) 175214.
[50] S.M. El-Refaei, D.L. Rauret, A.G. Manjón, I. Spanos, A. Zeradjanin, S. Dieckhöfer, J. Arbiol, W. Schuhmann, J. Masa, Ni-Xides (B, S, and P) for Alkaline OER: shedding light on reconstruction processes and interplay with incidental Fe impurities as synergistic activity drivers, ACS Appl. Energy Mater. 7 (2024) 1369–1381.
[51] C. Huang, Q. Zhou, D. Duan, L. Yu, W. Zhang, Z. Wang, J. Liu, B. Peng, P. An, J. Zhang, L. Li, J. Yu, Y. Yu, The rapid self-reconstruction of Fe-modified Ni hydroxysulfide for efficient and stable large-current-density water/seawater oxidation, Energy Environ. Sci. 15 (2022) 4647–4658.
[52] Y. Wang, S. Tao, H. Lin, G. Wang, K. Zhao, R. Cai, K. Tao, C. Zhang, M. Sun, J. Hu, B. Huang, S. Yang, Atomically targeting NiFe LDH to create multivacancies for OER catalysis with a small organic anchor, Nano Energy 81 (2021) 105606.
[53] H. Yang, C. Wang, Y. Zhang, Q. Wang, Green synthesis of NiFe LDH/Ni foam at room temperature for highly efficient electrocatalytic oxygen evolution reaction, Sci. China Mater. 62 (2019) 681–689.
[54] X.-J. Zhai, Q.-X. Lv, J.-Y. Xie, Y.-X. Zhang, Y.-M. Chai, B. Dong, Advances in the design of highly stable NiFe-LDH electrocatalysts for oxygen evolution in seawater, Chem. Eng. J. 496 (2024) 153187.
[55] Y. Sun, H. Dang, X. Li, J. Luan, D. Jiang, J. Mu, Y. Yang, Enhanced thermal conductivity of PEEK based composites fabricated by its fibers grafted graphene oxide, Colloids Surf. A Physicochem. Eng. Asp. 683 (2024) 132783.
[56] Z. Li, Y. Yao, S. Sun, J. Liang, S. Hong, H. Zhang, C. Yang, X. Zhang, Z. Cai, J. Li, Y. Ren, Y. Luo, D. Zheng, X. He, Q. Liu, Y. Wang, F. Gong, X. Sun, B. Tang, Carbon oxyanion self-transformation on NiFe oxalates enables long-term ampere-level current density seawater oxidation, Angew. Chem. Int. Ed. 63 (2024) e202316522.
[57] G. Mu, G. Wang, Q. Huang, Y. Miao, D. Wen, D. Lin, C. Xu, Y. Wan, F. Xie, W. Guo, R. Zou, A Kinetic control strategy for one-pot synthesis of efficient bimetallic metal-organic framework/layered double hydroxide heterojunction oxygen evolution electrocatalysts, Adv. Funct. Mater. 33 (2023) 2211260.

[58] H. Liu, W. Shen, H. Jin, J. Xu, P. Xi, J. Dong, Y. Zheng, S.-Z. Qiao, High-performance alkaline seawater electrolysis with anomalous chloride promoted oxygen evolution reaction, Angew. Chem. Int. Ed. 62 (2023) e202311674.
[59] L. Yu, L. Chi, Y. Wang, M. Ning, E. Nasr, S. Song, J. Luan, S. Chen, Z. Ren, Room-temperature-fabricated large-area catalysts for ampere-scale seawater oxidation, ACS Energy Lett. 10 (2025) 5664–5673.
[60] Y. Pei, D. Li, C. Qiu, L. Yan, Z. Li, Z. Yu, W. Fang, Y. Lu, B. Zhang, High-entropy sulfide catalyst boosts energy-saving electrochemical sulfion upgrading to thiosulfate coupled with hydrogen production, Angew. Chem. Int. Ed. 63 (2024) e202411977.
[61] M. Yue, X. He, S. Sun, Y. Sun, M.S. Hamdy, M. Benaissa, A.A.M. Salih, J. Liu, X. Sun, Co-doped Ni_3S_2 nanosheet array: a high-efficiency electrocatalyst for alkaline seawater oxidation, Nano Res. 17 (2024) 1050–1055.
[62] W. Xu, Z. Wang, P. Liu, X. Tang, S. Zhang, H. Chen, Q. Yang, X. Chen, Z. Tian, S. Dai, L. Chen, Z. Lu, Ag nanoparticle-induced surface chloride immobilization strategy enables stable seawater electrolysis, Adv. Mater. 36 (2024) 2306062.